Supporting Information

High Quantum Yield NIR Emission via Charge Transfer States in Buckybowl-TPA based D–A System

Yumi Yakiyama,*[a,b,c] Junyi Han,[a] Hayato Sakai,*[d] Taku Hasobe,[d] Youhei Takeda,[a] Ryohei Kishi[b,e] Kei Ohkubo[f,g] and Hidehiro Sakurai*[a,b]

[a]*Division of Applied Chemistry, Graduate School of Engineering, The University of Osaka, 2-1 Yamadaoka, Suita, Osaka 565-0871, JP*
[b]*Innovative Catalysis Science Division, Institute for Open and Transdisciplinary Research Initiatives (ICS-OTRI), The University of Osaka, 2-1 Yamadaoka, Suita, Osaka 565-0871, JP*
[c]*PRESTO, Japan Science and Technology Agency (JST), Kawaguchi, Saitama 332-0012, JP*
[d]*Department of Chemistry, Faculty of Science and Technology, Keio University, Yokohama, Kanagawa 223-8522, JP*
[e]*Department of Materials Engineering Science, Graduate School of Engineering Science, The University of Osaka, Toyonaka, Osaka 560-8531, JP*
[f]*Institute for Open and Transdisciplinary Research Initiatives (OTRI), The University of Osaka, 1-6 Yamadaoka, Suita, Osaka 565-0871, JP*
[g]*Organization for Carbon Neutrality Collaboration (OCNC), The University of Osaka, 1-6 Yamadaoka, Suita, Osaka 565-0871, JP*

Table of Contents

1) General

Methods and Materials

All the chemical reagents and solvents were commercially purchased and purified according to the standard methods, if necessary. Air- and moisture-sensitive reactions were carried out using commercially available anhydrous solvents under inert atmosphere of nitrogen. Unless otherwise noted. ^{1}H and ^{13}C NMR spectra were recorded on a JEOL JNM-ECS400 NMR spectrometer (^{1}H: 400 MHz and ^{13}C: 100 MHz). Chemical shift (δ) are expressed relative to the resonances of the residual non-deuterated solvent for ^{1}H ($CDCl_3$: $^{1}H(\delta)$ = 7.26 ppm) and for ^{13}C ($CDCl_3$: $^{13}C(\delta)$ = 77.0 ppm). High resolution mass spectra (HRMS) were measured using electron impact mode (EI) methods on JEOL JMS-777V spectrometer. matrix-assisted laser desorption/ionization coupled to time-of-flight (MALDI-TOF) mass spectra were measured on Bruker Autoflex III spectrometer. The preparative TLC (PTLC) purification was conducted using Wako gel B-5F PTLC plates. Flash column chromatography was prepared using Kanto Silica gel 60N (neutral, spherical, 40-50 μm) and performed with a Yamazen preparative medium-pressure liquid chromatography system. UV-vis spectra were recorded on a JASCO V-670 spectrophotometer. Steady-state emission spectra were recorded on JASCO FP-6500DS and HORIBA Fluoromax-4 spectrometers. Phosphorescence, prompt fluorescence (PF), and delayed fluorescence (DF) spectra and decays were recorded using nanosecond gated luminescence and lifetime measurements (from 400 ps to 1 s) using either third harmonics of a high energy pulsed DPSS laser emitting at 355 nm (Q-Spark A50-TH-RE). Electron spin resonance spectrum was recorded on JEOL JES-X310 at 123 K after 365 nm light irradiation using 60 W LED.

Electrochemical characterization

Cyclic voltammetry (CV) was measured using Hokuto Denko HZ-7000 voltammetric analyzer at room temperature with a conventional three-electrode configuration consisting of a glass carbon working electrode, a platinum wire auxiliary electrode and an Ag wire pseudo-reference electrode with ferrocene–ferrocenium (Fc/Fc^{+}) as the internal standard. Nitrogen purged acetonitrile was used as solvent for scanning the oxidation with tetrabutylammonium perchlorate (TBAP) (0.1 M) as the supporting electrolyte. The cyclic voltammograms were obtained at a scan rate of 100 mV s^{-1}.

Transient absorption measurements

Femtosecond transient absorption measurements

The transient absorption spectroscopy measurements were carried out using a home-made femtosecond pump−probe system. Yb laser (PHAROS PH2-10W, Light Conversion) was used to create fundamental light pulses at 1030 nm at a repetition rate of 1 kHz. The pulse energy was 200 μJ, and the pulse duration was approximately 290 fs. 65% of the fundamental beam was directed to ORPHEUS optical parametric amplifier (Light Conversion) to produce excitation pulses at the desired wavelength or utilized to generate SHG (515 nm) and THG (343 nm) for sample pumping. The rest of the beam was delivered to a delay stage then attenuated appropriately and focused onto liquid D_2O or a sapphire crystal to generate a stable white light continuum for sample probing. The probe light was introduced to polychromators S3 equipped with a CMOS array (USP-PSMM-PK120, Unisoku) for the visible part of the spectrum and an InGaAs diode array (USP-NIR-PDA256,

Unisoku) for the near-infrared (NIR) wavelengths. The measurements were carried out by comparing responses with and without excitation using a chopper synchronized with the fundamental laser pulses. The spectra were typically acquired by recording 2000 shots, that is, averaging over 2 s. Excitation energies were sufficiently lowered to avoid multiple exciton generation; this was verified by recording a series of measurements with different excitation energies for the same sample. No excitation energy dependence of the response was observed.

Picosecond Transient Absorption Measurement[S1]

Picosecond transient absorption measurement (picoTAS, Unisok, Osaka, Japan) was conducted by the device made by Unisoku Co., Ltd. Measurement method used in this measurement was Randomly Interleaved Pulse Train Method.

Nanosecond transient absorption measurements

Nanosecond transient absorption measurements were carried out using Unisoku TSP-2000 flash spectrometer. Surelite-I Nd-YAG (Q-switched) laser was employed for the flash photo-irradiation. A 150 W Xenon arc and halogen lamps were used as the monitor light source.

Quantum yield calculation

A relative value of quantum yield was obtained by following relationship with using the corrected spectra data JASCO Spectra Manager™.

$$\Phi_u = \Phi_{st} \cdot \left(\frac{F_u}{F_{st}}\right) \cdot \left(\frac{A_{st}}{A_u}\right) \cdot \left(\frac{D_u}{D_{st}}\right) \cdot \left(\frac{I_{ex,st}}{I_{ex,u}}\right) \cdot \left(\frac{{n_u}^2}{{n_{st}}^2}\right)$$

Here, F_{st} is the fluorescence quantum yield for the standard sample; F_u and F_{st} are the integrated values for the emission spectra of the unknown and standard samples; A_{st} and A_u are the absorbance at the excitation wavelength of the standard and unknown samples; $I_{ex,st}$ and $I_{ex,u}$ are the intensities of the excitation light at the excitation wavelengths for the standard and unknown samples; and n_u and n_{st} are the average refractive indexes for the emission spectra measurement range for the standard and unknown samples.

In this measurement, Tris(2,2'-bipyridyl)Ru(II) hexahydrates as the reference (QY = 0.55).[S2] Sample concentrations were low enough (less than 10% absorption across the spectrum) and the same sample solutions were used in both absorption and emission spectra measurements. Also, $I_{ex,st}/I_{ex,u}$ was corrected automatically in the software and considered to be 1.0. Therefore, the above equation becomes:

$$\Phi_u = \Phi_{st} \cdot \left(\frac{F_u}{F_{st}}\right) \cdot \left(\frac{A_{st}}{A_u}\right) \cdot \left(\frac{{n_u}^2}{{n_{st}}^2}\right)$$

Global and Target Analysis

Global (singular value decomposition-based) and target (differential equation-based) analysis is accomplished using the Glotaran software package (http://glotaran.org).[S3]

Dipole moment of ground (μ_g) and excited state (μ_e)

The Stokes shift is determined as the difference in wavenumber between the lowest energy absorption and the highest energy florescence band. Estimates of these values obtained experimentally using the Lippert−Mataga equation.[S4]

$$\Delta v = \left[2(\mu_e - \mu_g)^2/hca^3\right]\Delta f + v^0$$

$$\Delta f = [(\varepsilon - 1)/(2\varepsilon + 1)] - \left[(n^2 - 1)/(2n^2 + 1)\right]$$

Where Δv is Stokes shift, the superscript "0" indicates the absence of solvent, μ_g and μ_e are dipole moments in the ground state and the excited state, respectively, *a* is Onsager cavity radius, here the value gets from gaussian calculation. ε and *n* are solvent dielectric constant and refractive index respectively.

The Onsager cavity radius and, Ground-state and Singlet excited state dipole moments (in Debye, D).

	Onsager cavity radius (Å)	μ_g[a]	μ_e[b]	μ_e[c]
TPA-TOS	6.57	3.41	33.32	54.27

[a]Ground-state dipole moment estimated by Gaussian software.

[b]Excited-state dipole moment estimated by Gaussian software.

[c]Excited-state dipole moment calculated from equation.

Calculate spin-spin distance

Spin-spin distance *r* in 3CS state of TPA-TOS was estimated from the EPR *D* value (triplet ZFS) with using the point-dipole approximation.[S5]

$$|D| = \frac{\mu_0 g^2 \mu_B^2}{4\pi \quad h \quad r^3} 1 \Rightarrow r \propto |D|^{-1/3}$$

If *D* is in mT:

$$r(\text{Å}) \approx \left(\frac{52040}{28.025|D(mT)|}\right)^{1/3}$$

2) Synthetic details

Synthesis of TPA-TOS

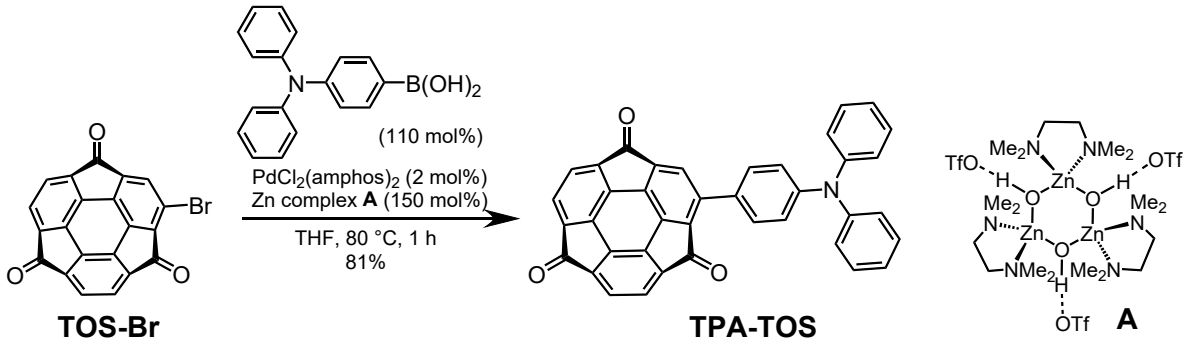

Scheme S1. Synthesis of **TPA-TOS**.

2-(4-(diphenylamino)phenyl)-1H-tricyclopenta[def,jkl,pqr]triphenylene-1,4,7-trione (TPA-TOS)

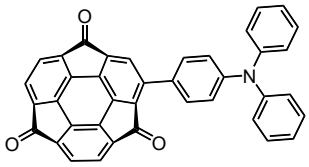

To a 4 mL test tube equipped with a magnetic stir bar were added **TOS-Br**[S6] (38.6 mg, 0.10 mmol), 4-(diphenylamino)phenylboronic acid (34.7 mg, 0.12 mmol), $PdCl_2$(amphos)2 (1.4 mg, 2.0 μmol), Zn complex **A**[S7] (52.1 mg, 0.15 mmol), and THF (1.0 mL). The mixture was stirred for one hour at 80 °C and then cooled to room temperature. The mixture was extracted with DCM (ca. 3 mL × 3). The combined organic extract was dried over Na_2SO_4. After filtration, the filtrate was concentrated under reduced pressure. The residue was purified by PTLC (CH_2Cl_2) to give the green solid.

R_f = 0.55 (CH_2Cl_2); m.p.: 400 °C (dec.); ^{1}H NMR (600 MHz, Chloroform-*d*, ppm): δ = 7.63 (s, 1H), 7.52 (d, *J* = 11.2 Hz, 2H), 7.43 (d, *J* = 7.3 Hz, 1H), 7.40 (d, *J* = 8.0 Hz, 1H), 7.38 (d, *J* = 9.6 Hz, 1H), 7.37 (d, *J* = 7.7 Hz, 1H), 7.31 (t, *J* = 7.7 Hz, 4H), 7.19 (d, *J* = 7.7 Hz, 4H), 7.11 (t, *J* = 7.3 Hz, 2H), 7.09 (d, *J* = 8.4 Hz, 2H); ^{13}C NMR (150 MHz, Chloroform-*d*, ppm): δ = 188.74, 188.48, 186.97, 150.67, 150.48, 149.83, 149.10, 148.88, 147.06, 146.30, 144.50, 144.08, 143.96, 143.57, 143.33, 136.94, 131.04, 129.67, 129.19, 128.38, 128.31, 126.71, 126.62, 126.49, 126.34, 125.92, 125.79, 124.25, 120.95; IR (ATR, cm^{-1}): $\tilde{\nu}$ = 2938, 2923, 2851, 1716, 1589, 1561, 1512, 1488, 1329, 1286, 1193, 1181, 951, 756, 746, 697; HRMS (EI): *m*/*z* Calcd. for $C_{39}H_{19}NO_3^+$: 549.1365 $[M]^+$; found: 549.1360.

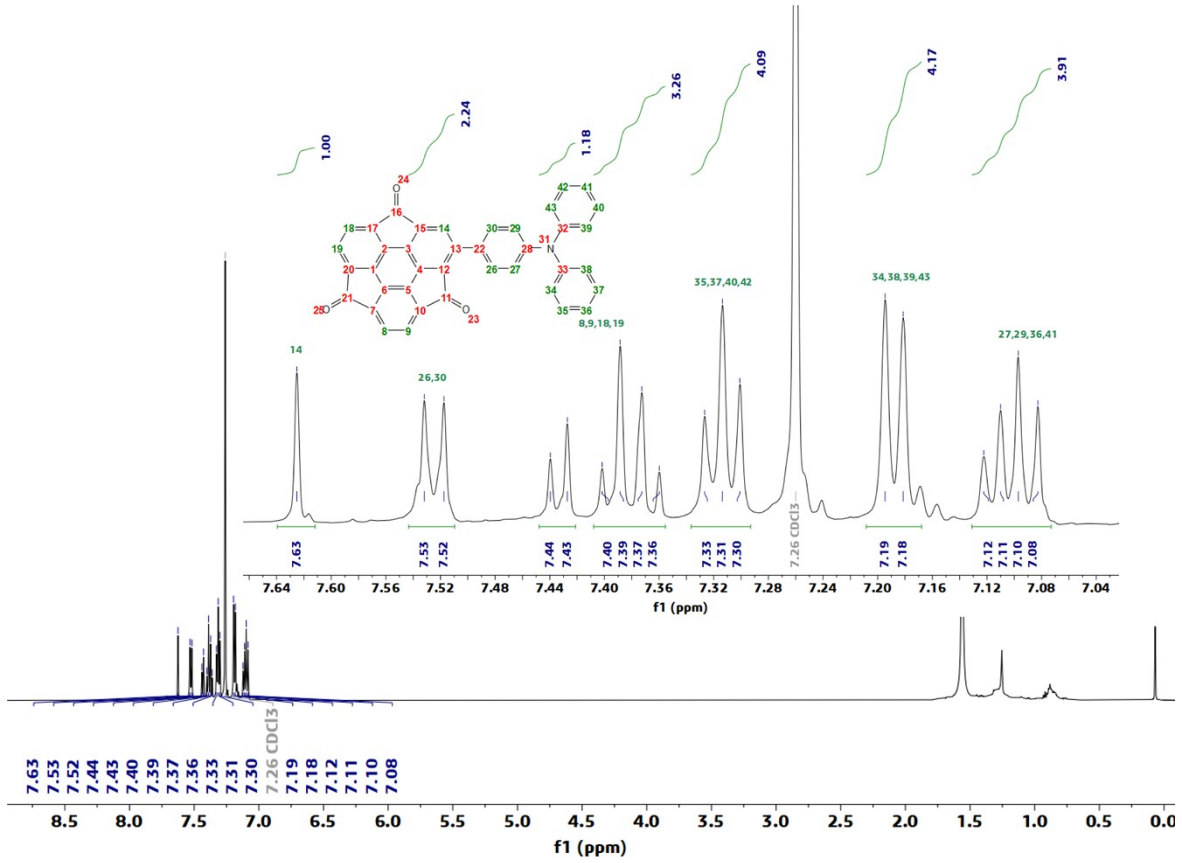

NMR Spectrum S1. ^{1}H NMR spectrum of **TPA-TOS** (600 MHz, Chloroform-*d*, 300 K).

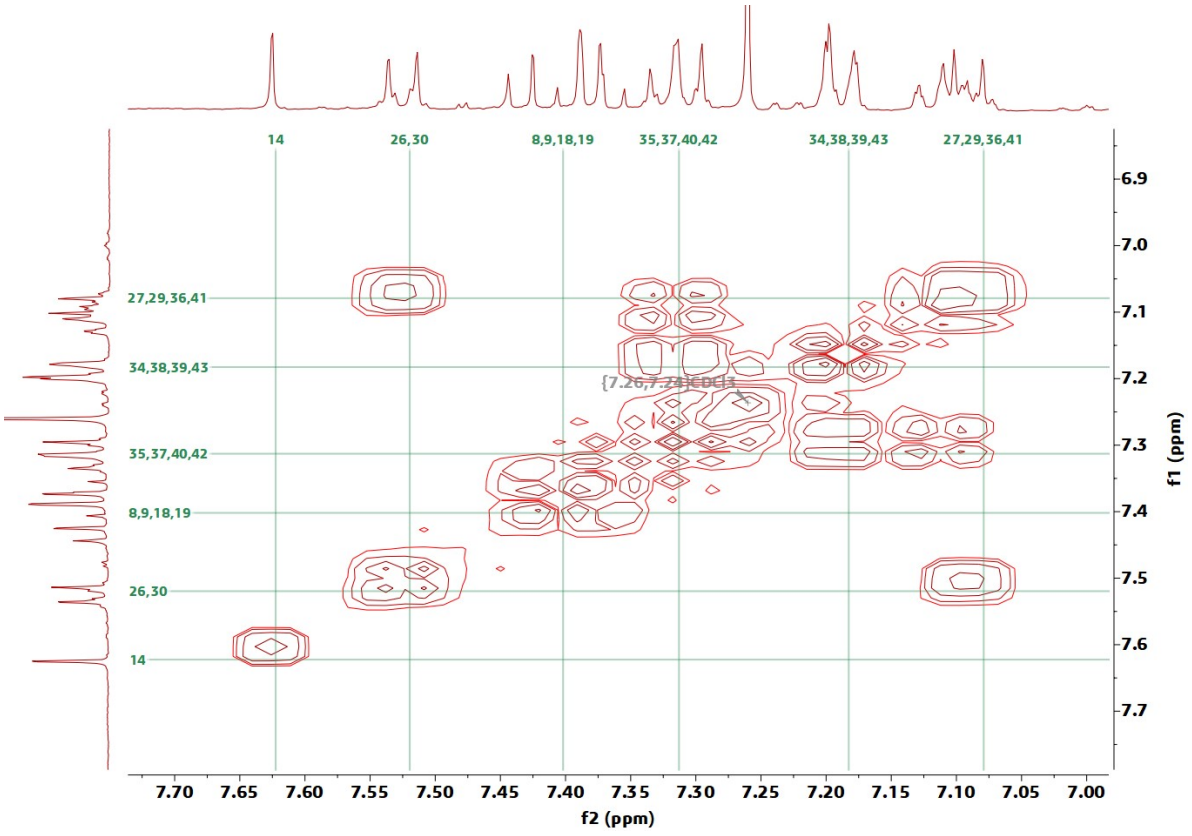

NMR Spectrum S2. 2D NMR Correlation (COSY) spectra of **TPA-TOS** aromatic region in chloroform-*d*

at 300 K.

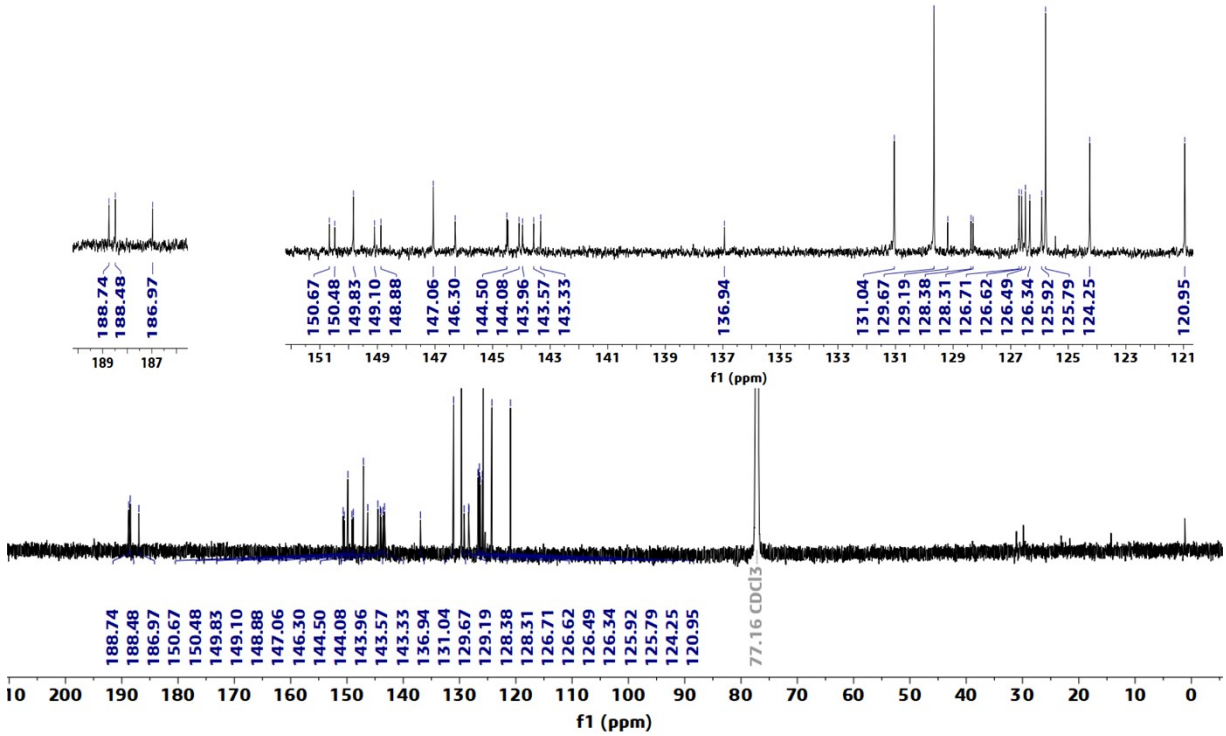

NMR Spectrum S3. ^{13}C NMR spectrum of **TPA-TOS** (150 MHz, Chloroform-*d*, 300 K).

3) Supplementary Figures and Tables

Table S1. Photophysical Properties of **TOS** and **TPA-TOS** in various solvents (c = 1.0 × 10^{-5} M) at 300 K.

	Solvents	l_{abs} [nm] (ε [10^4·M^{-1}·cm^{-1}])	l_{em} [nm][a] (Ψ_{em})
TPA-TOS	Hexane	296 (6.1), 643 (1.2)	703 (0.66, 0.34[b])
	Benzene	292 (6.7), 652 (1.2)	393 (0.05)
	PhCN	302 (7.1), 653 (1.2)	354 (0.02)
	MCH	301 (7.5), 652 (1.2)	355 (0.12), 703(0.07)
	MeCN	300(7.6), 662 (1.2)	355 (0.01)
	Zeonex[c]	304, 665	739 (0.74)
	PMMA[c]	300, 644	732 (0.32)

[a]λ_{ex} = 300 nm in N_2. [b]Tested under an O_2 atmosphere. [C]0.5 wt%.

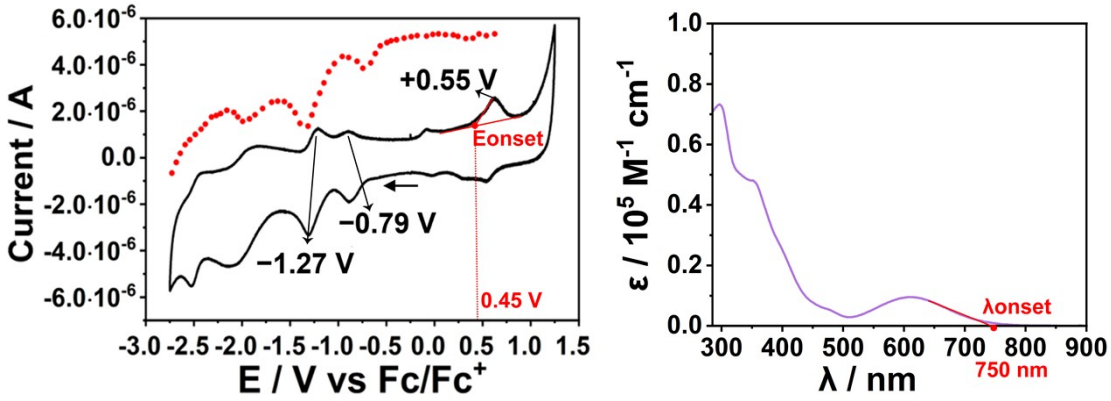

Figure S1. Redox properties evaluated by cyclic voltammetry (solid black line) and differential pulse voltammetry (red dotted line) of 1 mM of **TPA-TOS** (10^{-3} M, vs. Fc/Fc^+) in 0.1 M Bu_4NClO_4 in MeCN electrolyte at the scan rate of 100 m V/s. Illustration of the procedures used for finding the onset oxidation potential E_{onset} (left) and the onset wavelength λ_{onset} (right), respectively, from the CV and UV-vis spectrum.

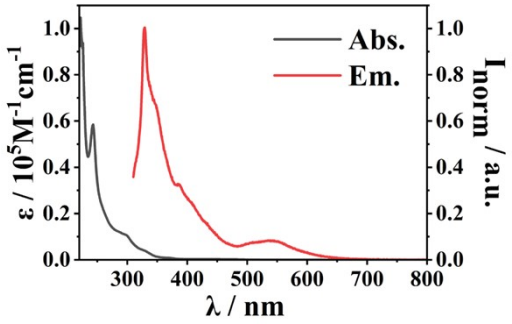

	condition	l_{abs} [nm] (ε [10^4·M^{-1}·cm^{-1}])	l_{em} [nm][a] (Ψ_{em})
TOS	DCM	228 (5.8), 300 (1.1)	330 (0.02)

[a]λ_{ex} = 300 nm in N_2.

Figure S2. UV–vis absorption and PL spectra (l_{ex} = 300 nm) of **TOS** in DCM (c = 1.0 × 10^{-4} M) at 300 K.

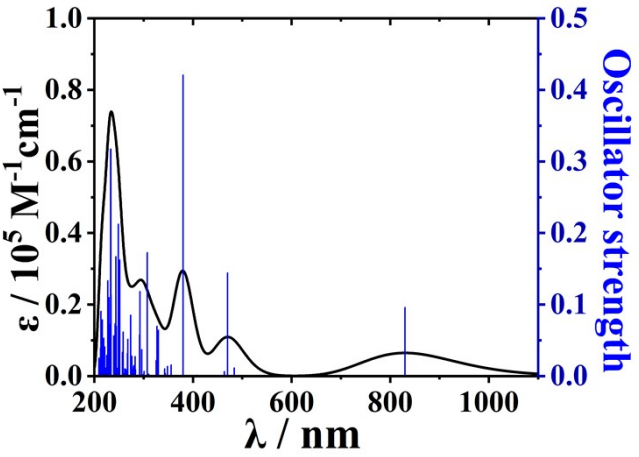

Figure S3. Simulated UV-vis spectrum of **TPA-TOS** calculated at B3LYP/6-311G** level of theory.

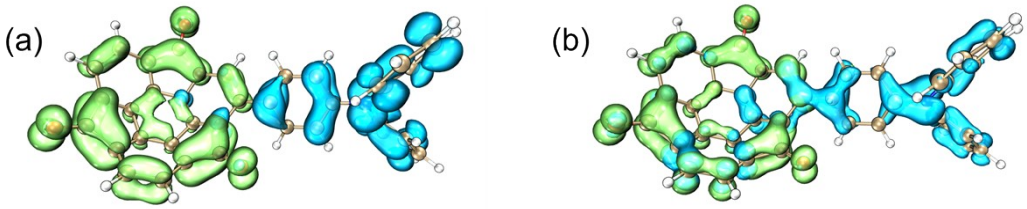

Figure S4. Isosurfaces of hole and electron distribution of **TPA-TOS** corresponding to (a) 600-800 nm ($S_0 \rightarrow S_1$) and (b) 300 nm ($S_0 \rightarrow S_{52}$) absorptions calculated at B3LYP/6-311G** level of theory. The blue and green isosurfaces indicate hole and electron distributions, respectively.

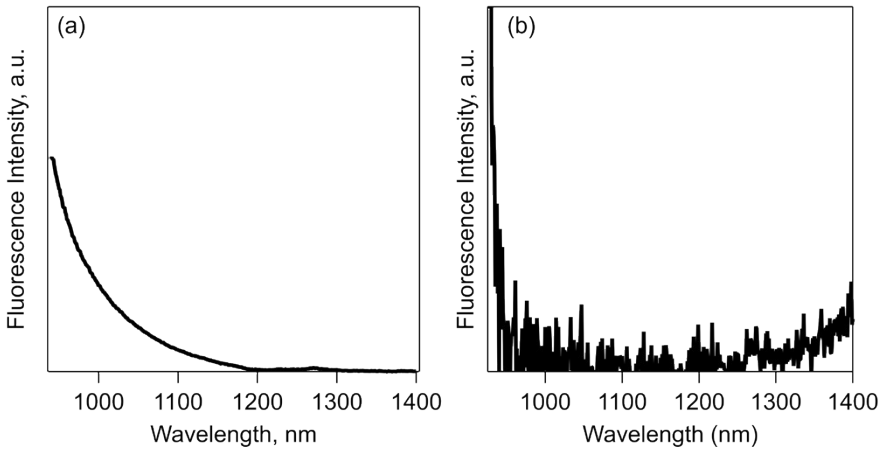

Figure S5. PL spectra (I_{ex} = 300 nm) of **TPA-TOS** in (a) hexane and (b) MeCN (c = 1.0 × 10^{-5} M) at 300 K.

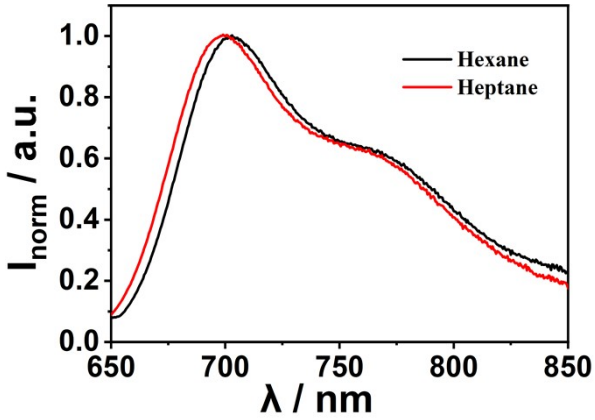

Figure S6. PL spectra (l_{ex} = 650 nm) of **TPA-TOS** in nonpolar solvents (c = 1.0 × 10^{-5} M) at 300 K.

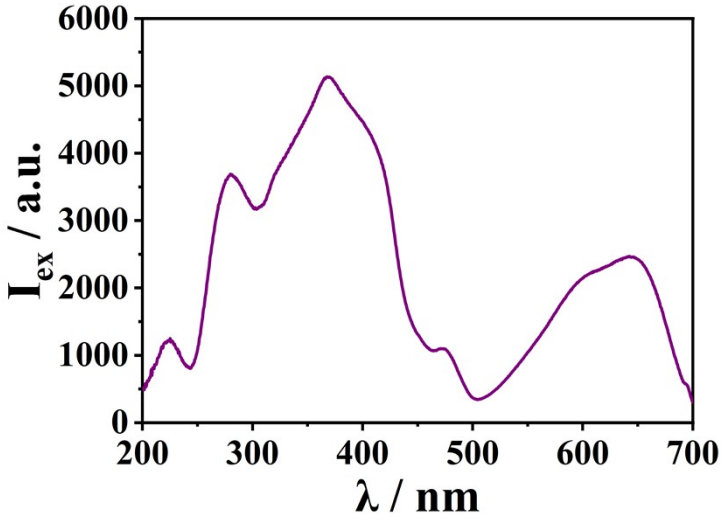

Figure S7. Excitation spectra (l_{em} = 750 nm) of **TPA-TOS** in hexane at 300 K (c = 1.0 × 10^{-5} M).

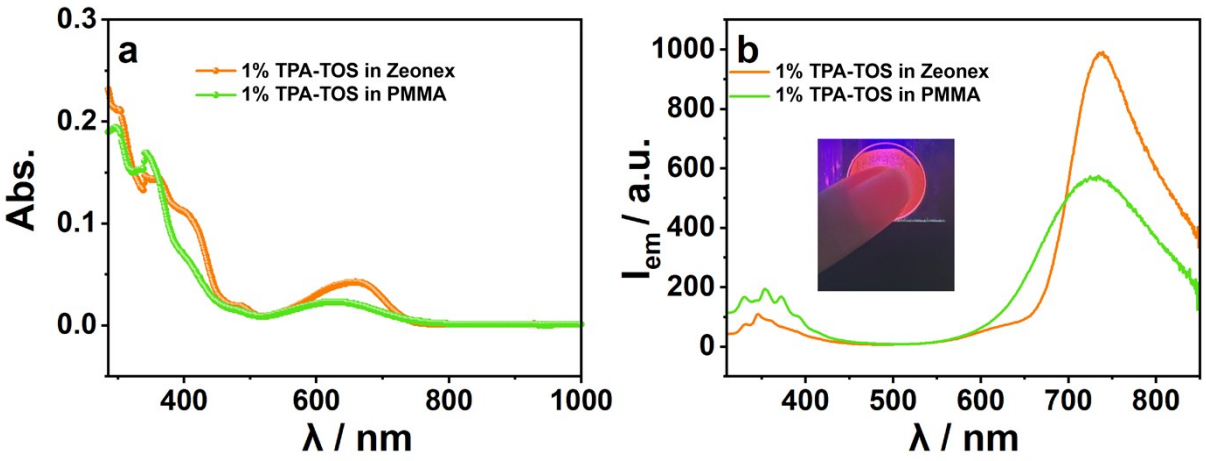

Figure S8. UV−vis-NIR absorption spectra (a) and PL spectra (I_{ex} = 300 nm) (b) of **TPA-TOS** (1 wt%) in doped PMMA and Zeonex film at 300 K. The inset image was 1% **TPA-TOS** Zeonex film taken under UV lamp (I_{ex} = 365 nm) irradiation.

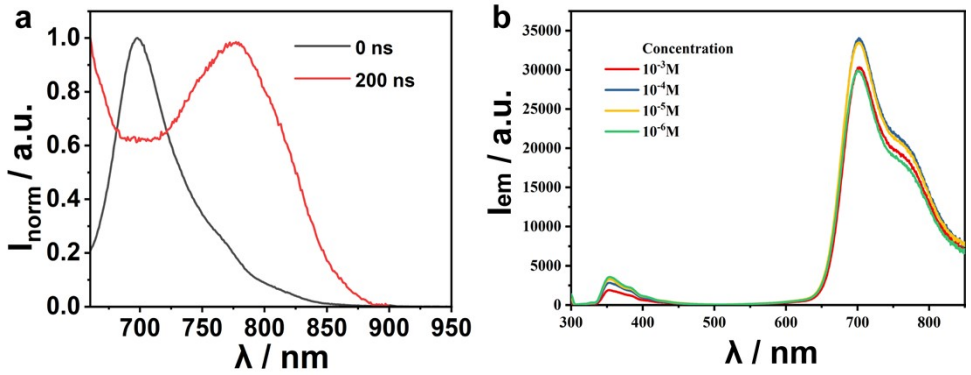

Figure S9. (a) Delayed emission spectra of **TPA-TOS** collected 200 ns after excitation at 650 nm in hexane (c = 1.0 x 10^{-5} M). (b) Emission spectra of **TPA-TOS** with different concentration in hexane.

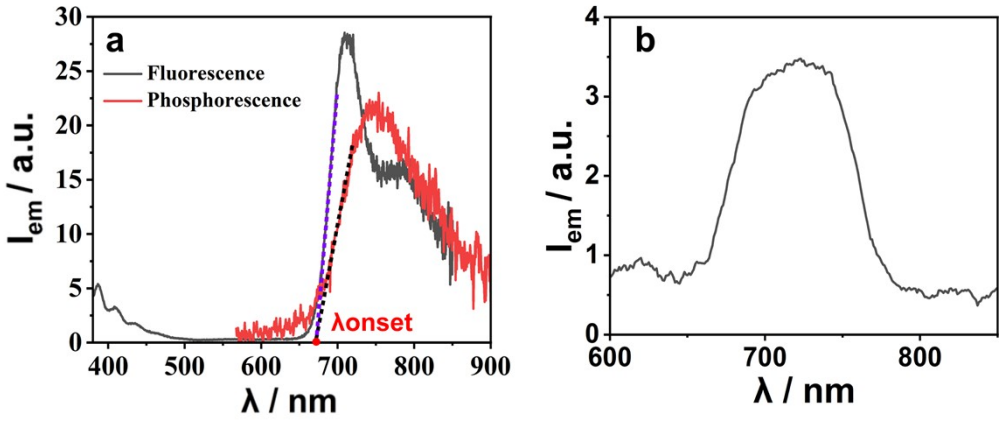

Figure S10. a) Emission spectrum of **TPA-TOS** (c = 110^{-3} M, I_{ex} = 300 nm) in 2Me-THF glass at 77 K. b) Phosphorescence spectrum of **TPA-TOS**-doped Zeonex film (I_{ex} = 300 nm) at 300 K.
The onset positions were determined by the intersection of the tangent to the low-energy edge of each emission spectrum with the baseline. ΔE_{st} was then calculated from the difference between the corresponding singlet and triplet energies using the relation $E = hc/\lambda$.

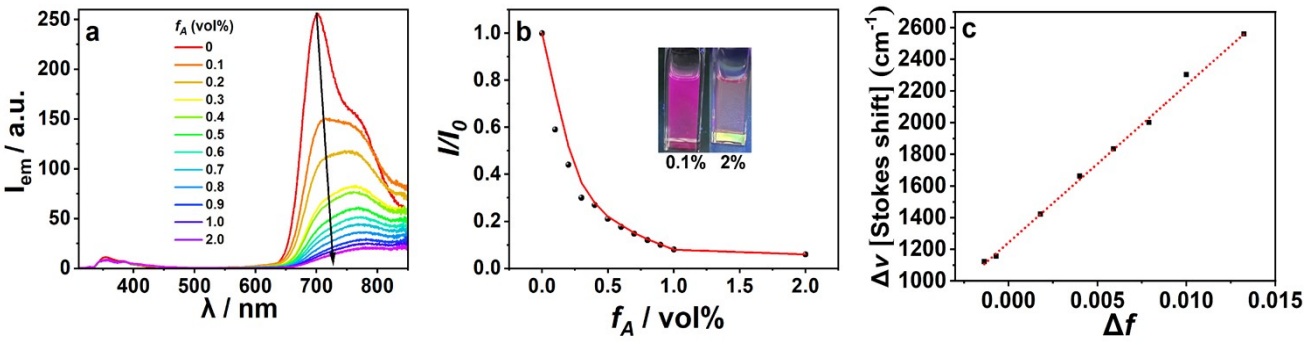

Figure S11. Emission spectra of **TPA-TOS** with the increase of volume fraction of MeCN in hexane (f_A). λ_{ex} = 300 nm, c = 1 × 10^{-5} M. (a) Emission intensity change against f_A. (b) I/I_0 values versus f_A of MeCN. Here, I_0 and I are the emission intensity in pure hexane and each hexane/MeCN mixture, respectively. Inset image shows the emission change depending on the f_A value under 365 nm UV light. (c) The Lippert–Mataga plot for **TPA-TOS**.

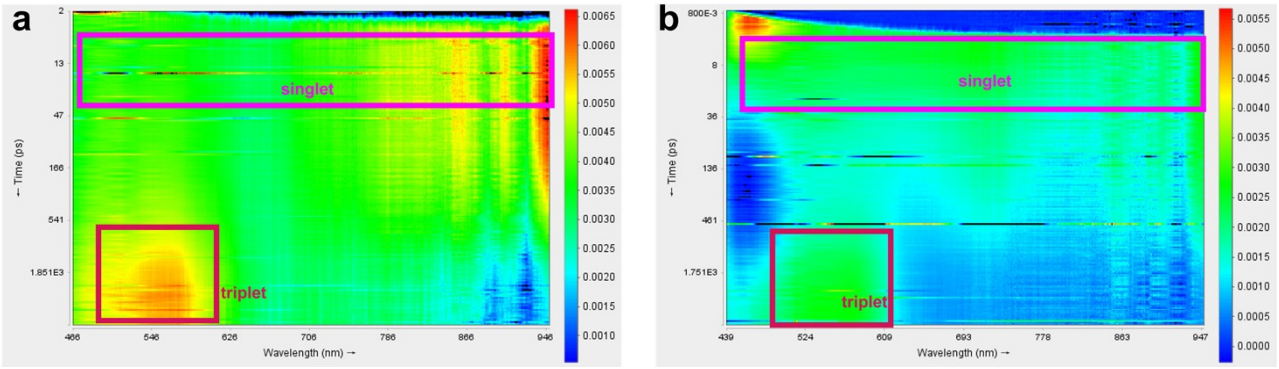

Figure S12. Femtosecond transient absorption map of **TOS** (c = 1.0 × 10^{-5} M, l_{ex} = 343 nm) in deaerated a) toluene and b) MeCN at 300 K. It was impossible to get the data in hexane due to the sample solubility.

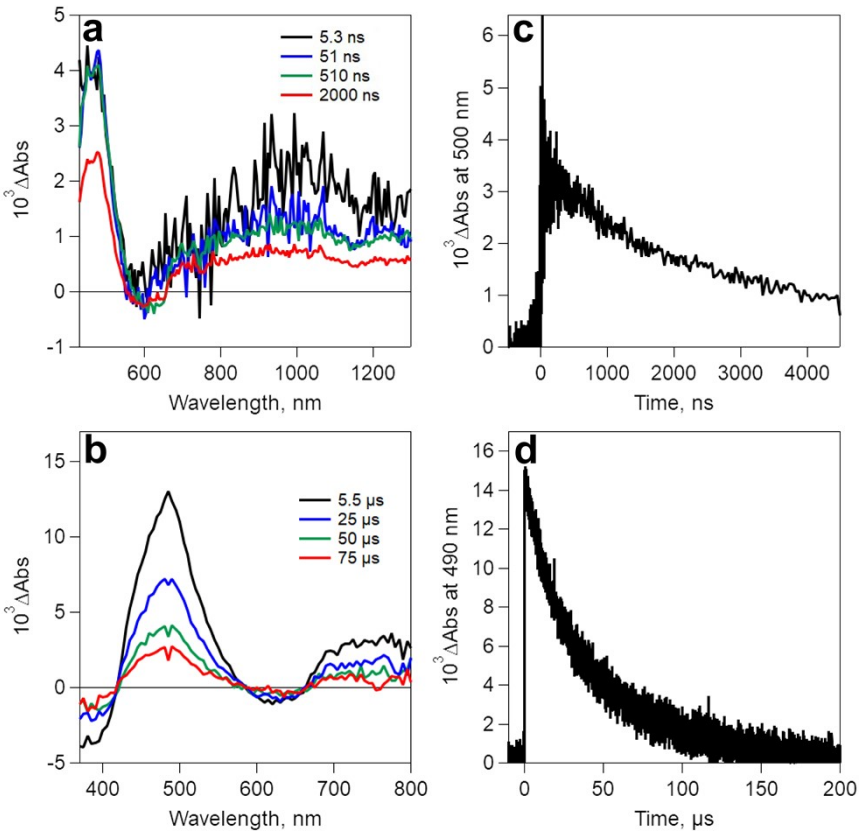

Figure S13. Picosecond (a) and nanosecond (b) transient absorption spectra and corresponding time profiles (c) and (d) of **TPA-TOS** in deaerated hexane after laser excitation at 355 nm (c =10^{-3} M).

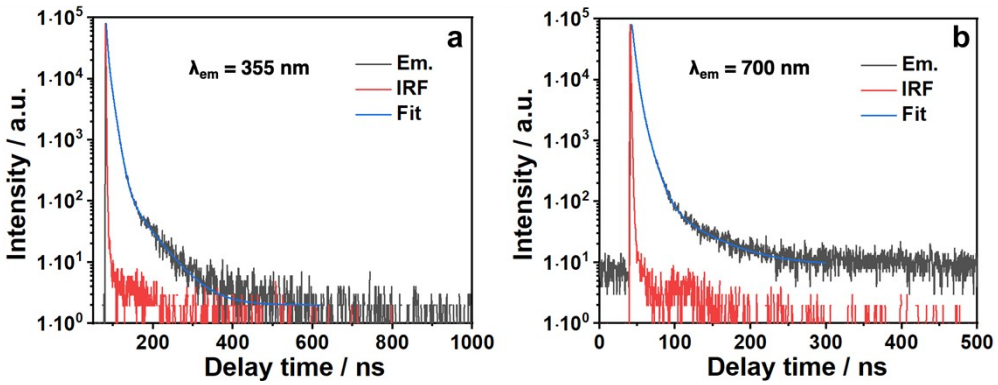

Figure. S14. Time-resolved fluorescence emission (λ_{ex} = 280 nm) for **TPA-TOS** in ZEONEX® film at 300 K under air.

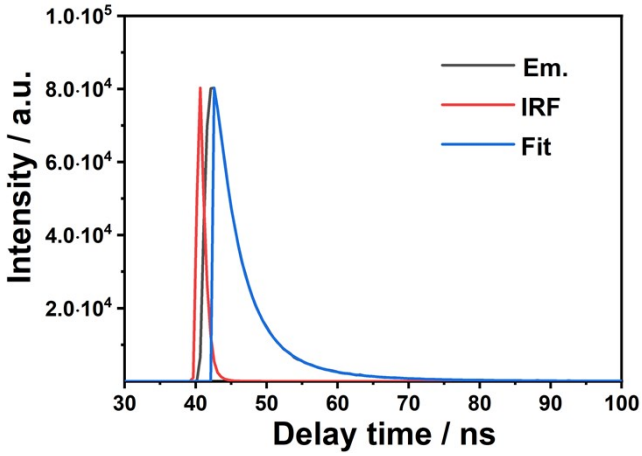

Figure. S15. Time-resolved fluorescence emission (λ_{ex} = 280 nm) for **TPA-TOS** in MeCN at 300 K under N_2.

4) Theoretical calculations

The preliminary calculation data of molecular geometry of S_0 state were optimized by density functional theory (DFT), and the geometries of S_1, T_1 states were optimized by time-dependent DFT (TDDFT) at the B3LYP/6-311G** level with the Gaussian-16 program.[S8] Isosurfaces of hole and electron distribution, were generated by Multiwfn.[S9,10] The approximate optimization results reveal that the molecular will twist in the excited states. Thus, the efficient intersystem crossing (ISC) or reverse ISC process should be ascribed to a twist structure in the excited state.

To test if the assumption of fast equilibration between the singlet and triplet manifold holds, the rate of ISC and rISC has to be estimated. We only consider the direct T_1 to S_1 transition, because calculation of T2 and S2 have a large energy gap with T_1 and S_1, so neglecting the intersystem crossing. And for this purpose, employ the Fermi Golden Rule approximation in combination with a Marcus formalism to estimate the density of states from the reorganization energy λ and the driving force ΔE according to the equation. [S11]

$$k = \frac{2\pi}{\hbar}\left|\langle\psi_f|\hat{H}_{SO}|\psi_i\rangle\right|^2 \sqrt{\frac{1}{4\pi\lambda k_b T}} exp\left(-\frac{(\Delta E_{ST}+\lambda)^2}{4\lambda k_b T}\right)$$

Here, ħ is the Planck constant, k_b is the Boltzmann constant and T is the temperature. $\langle\psi_f|\hat{H}_{SO}|\psi_i\rangle$ spin-orbit coupling between the initial and final adiabatic electronic states. When calculate k_{ISC}, λ corresponds to the difference between the vertical energy of the final state (here T1) at the geometry and in the solvent field (non-equilibrium regime) of the initial state (here S1) and its adiabatic energy. When calculate k_{ISC}, λ corresponds to the difference between the vertical energy of the final state (here S1) at the geometry and in the solvent field (non-equilibrium regime) of the initial state (here T1) and its adiabatic energy, while the driving force ΔE_{ST} is identified as the adiabatic singlet–triplet gap. SOC is calculated by using the ORCA with the effective charge approximation of the Breit-Pauli self-selected orbital Hamiltonian.[S12]

Calculation of excited state lifetime according to Einstein's formula.

$$\tau = \frac{3}{2fv^2}$$

Table S2 Calculated results of **TPA-TOS**.

	SOC(S_1-T_1) (cm^{-1})	ISC(s^{-1})	rISC(s^{-1})	lifetimeτ(s)	k_s(s^{-1})	lifetimeτ(t)	k_t(s^{-1})
S_1	0.01	1.25E+03	4.75E+02	1.03E-08	9.68E+07	-[a]	-
T_1	0.32	1.03E+06	3.73E+05	6.52E-07	1.53E+07	1.61E-01	6.20

[a] The oscillator strength is 0.

Difficulties in Theoretical Investigation of TPA-TOS

However, indeed, theoretical results of excitation properties for delocalized intramolecular CT systems depend on the level of approximation. Of course, there have been several benchmarking studies suggesting recommended calculation methods for excitation properties of intramolecular CT systems. Because of the extended π-conjugation system, the methodology dependence for the **TPA-TOS** was somewhat complicated.

Geometry optimization

First, we performed geometry optimization of **TPA-TOS** (in hexane) in the S_0 state at the RB3LYP/6-

311G(d,p) level with the SMD model for the environmental effects. Then, we simulated the electronic absorption spectrum at the TD-RB3LYP/6-311G(d,p) level, which reproduced well the position experimental CT band around 600-800 nm, although the excitation energy seems to underestimate to some extent. Usually, long-range corrected DFT functionals are recommended for the description of such CT bands. However, TD-RCAM-B3LYP/6-311G(d,p) overestimated significantly the excitation energies with the default range-separating parameter (μ = 0.33 bohr^{-1}). We also performed the calculations with a recently proposed global double hybrid functional, SOS-PBE-QIDH[S13], recommended for prediction of CT excitations in a benchmarking study by Mester et al.[S14] Among the employed methods, the TD-B3LYP, TD-RCAM-B3LYP(0.15) or TD-RCAM-B3LYP(0.10) seem to better reproduce the experimental absorption wavelength.

Table S3. TD-DFT vertical excitation energies for the T_1 and S_1 states of **TPA-TOS** using the hybrid and double hybrid functionals based on the S_0 geometry optimized at the RB3LYP/6-311G(d,p) level. Environmental effects of *n*-hexane solvent were considered using the SMD model for the regular hybrid functionals and the C-PCM model for the double hybrid functional. The 6-311G(d,p) basis set was used.

Functional	***E*(T$_1$) [eV]**	***E*(S$_1$) [eV] (λ [nm])**	**Δ*E*$_{ST}$ [eV]**
TD-RB3LYP	1.284	1.457 (851)	0.173
TD-RCAM-B3LYP(0.33)[#]	1.869	2.497 (497)	0.628
TD-RCAM-B3LYP(0.25)[#]	1.863	2.338 (530)	0.475
TD-RCAM-B3LYP(0.20)[#]	1.803	2.194 (565)	0.354
TD-RCAM-B3LYP(0.15)[#]	1.690	2.003 (619)	0.313
TD-RCAM-B3LYP(0.10)[#]	1.520	1.760 (705)	0.240
TD-SOS-PBE-QIDH[##]	2.293	2.324 (534)	0.031

[#] The values in round parenthesis denote the range-separating parameter μ [bohr^{-1}].
[##] A recently proposed global double hybrid functional[S13] recommended for the CT excitations in a benchmarking study.[S14] The "AutoAux" and "RIJCOSX" options in ORCA5 package were employed.

The dihedral angle (*θ*) dependence of relative energies

We also checked the dihedral angle (θ) dependence of relative energies of the S_0, T_1 and S_1 states. The TD-RB3LYP predicted the *θ*-dependent S_1-T_1 gap (ΔE_{ST}) and $\Delta E_{ST} \sim 0$ around θ = 90˚. However, it is found that the results of $E_{T1}(\theta)$, $E_{S1}(\theta)$, and $\Delta E_{ST}(\theta)$ depend strongly on the choice of functional. For the TD-RCAM-B3LYP results with μ ≥ 0.2 bohr^{-1}, ΔE_{ST} was non-zero around $\theta = 90˚$. Particularly, when we employed the TD-RCAM-B3LYP(0.33), $\Delta E_{ST}(\theta = 90˚) > \Delta E_{ST}(\theta = 30˚)$. Furthermore, the T_2 state was below the S_1 state around $\theta = 90˚$. The double hybrid TD-SOS-PBE-QIDH predicted negative ΔE_{ST} probably because the perturbative corrections for the S_1 and T_1 states were performed separately. Another issue is the S_1 potential energy curve. With the TD-RB3LYP method, the S_1 potential energy curve was very flat in the range $30˚ \le \theta \le 120˚$, and the geometry optimization for the S_1 state resulted in a geometry with $\theta \sim 90˚$. With the TD-RCAM-B3LYP(0.15) method, whose S_1 absorption wavelength (E_{S1} = 1.9992 eV, $\lambda_{abs,calc}$ = 620 nm, f = 0.1642, solvent: n-hexane) seems to reproduce well the experimental result, the S_1 potential energy curve was not so flat around the region and the geometry optimization for the S_1 state (the frequency analysis was not performed yet) resulted in a geometry with $\theta \sim 27˚$ (E_{S1} = 1.7389 eV, $\lambda_{em,calc}$ = 713 nm, f = 0.1623, solvent: *n*-hexane).

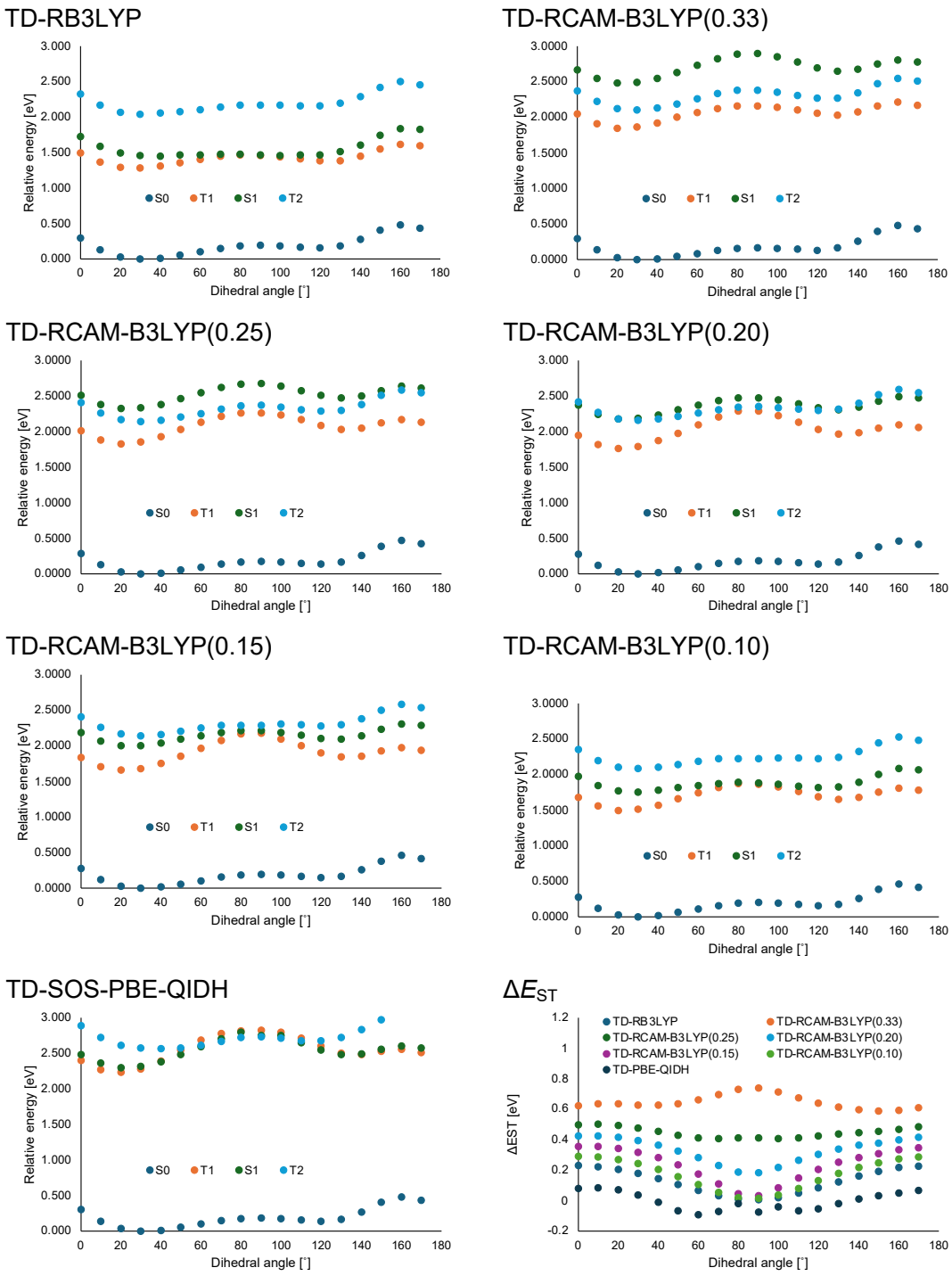

Figure S15. Dihedral angle (θ) dependence of the energies of the S_0, T_1, S_1 and T_2 states of **TPA-TOS** relative to the S_0 state energy at θ = 30˚ (solvent: n-hexane) and the results of $\Delta E_{ST}(\theta) = E_{S1}(\theta) - E_{T1}(\theta)$. The θ-dependent geometries were constructed based on the S_0 geometry optimized at the RB3LYP/6-311G(d,p) level, keeping the remaining geometrical parameters frozen. The 6-311G(d,p) basis set was used. There were some cases where T_3 was lower than S_1.

When the DFT-based results show such strong xc-functional dependences, we usually try to perform the wavefunction theory (WFT)-based methods, i.e., *ab initio* post-Hartree-Fock (HF) methods. However, we faced difficulty in conducting the post-Hartree-Fock methods because of the weak but non-negligible electron correlation effects in the S_0 state that could not be recovered appropriately from the perturbative correction to the spin-restricted (R)HF solution.

Table S4. Post-HF vertical excitation energies of **TPA-TOS** for the S_1 state based on the S_0 geometry optimized at the RB3LYP/6-311G(d,p) level.

Method	$E(S_1)$ [eV] (λ [nm])
RHF+RI-CC2/def2-SVP[#]	2.668 (465)
UHF+RI-CC2/def2-SVP[#†]	2.658 (466)
RHF+RI-CC2/def2-TZVP[#]	2.447 (507)
RHF+RI-CIS(D)/6-311G(d,p)[##]	2.651 (468)
SA5-CASSCF(4,4)+QD-NEVPT2/6-311G(d,p)[##]	2.202 (563)
SA5-CASSCF(6,6)+QD-NEVPT2/6-311G(d,p)[##]	2.474 (501)
SA5-CASSCF(8,8)+QD-NEVPT2/6-311G(d,p)[##]	2.384 (520)

[#] Calculations were performed using Turbomole 7.7 (gas phase calculation).
[##] Calculations were performed using ORCA 5.0.4. C-PCM was employed (solvent: n-hexane). SA*x*-CASSCF(*n*,*m*) represent that the state-averaged (SA-)CASSCF calculations were performed for the *x* singlet states with the *n*-electron and *m*-orbital complete active space.
[†]The BS-UHF solution (E_{tot} = -1765.6466007 a.u., $\langle S^2 \rangle$ = 4.09) was lower than the RHF solution (-1765.5899125 a.u., $\langle S^2 \rangle$ = 0.00).

When we performed the spin-unrestricted (U)HF calculation followed by the instability analysis for the UHF solution, we obtained the broken-symmetry (BS-)UHF solution with lower energy than the RHF solution. Although the diradical character y_0 at the spin-projected (P)UHF level was less than 0.1, meaning that the S_0 state is fairly "closed-shell", the solution showed high spin-contaminations with $\langle S^2 \rangle \sim 4$, because plural diradical characters y_0, y_1, y_2, … exhibited non-zero values. When y_0 of a system at the PUHF level is larger than ~0.5, the system can often be regarded as an "open-shell" system where partially unpaired electrons appear mainly due to the strong (static) electron correlation. In the present case, however, the RHF solution cannot be a good starting point for the post-HF calculations. We should note that usual hybrid DFT methods did not give the BS solutions (unless the fraction of Hartree-Fock exchange is ~ 100%).

When the post-RHF calculations did not work appropriately, the post-UHF or the multireference calculations may be candidates we should employ. Unfortunately, the former ones are considered not to give reliable results for the excited states because of the highly spin-contaminated reference state with $\langle S^2 \rangle \sim 4$. We need to set an appropriate active space for the latter ones, but there are plural non-zero but small diradical characters y_0, y_1, y_2, …, which indicates the difficulty in selecting active space. Indeed, when we performed the *x*-state averaged (SA*x*-)CASSCF(n,m) + QD-NEVPT2 calculations with different numbers of active electrons (n) and orbitals (m), but the results of S_1 excitation energy overestimated the experimental result.

Cartesian coordinates

Optimized cartesian coordinates of S_0 for trioxosumanene (**TOS**)

C	27.73232	-55.5781	0.424349	C	24.56269	-57.3335	0.469608
C	26.60524	-56.2403	0.835984	C	25.38117	-56.0588	0.193784
C	26.70984	-57.569	1.38359	C	25.30254	-55.101	-0.80645
C	27.93644	-58.1705	1.492394	C	26.4742	-54.4123	-1.23414
C	29.1215	-57.4744	1.059136	C	27.70189	-54.6946	-0.65374
C	29.02198	-56.2107	0.538447	C	29.13961	-54.6433	-1.20272
C	29.88675	-55.7669	-0.46096	H	31.59312	-56.3224	-1.65171
C	30.92931	-56.5991	-0.84106	H	31.77191	-58.5857	-0.7189
C	31.03293	-57.913	-0.29984	H	27.00733	-61.386	1.026499
C	30.092	-58.3695	0.611384	H	24.38836	-54.9619	-1.37136
C	29.54416	-59.7767	0.912331	H	26.40692	-53.7753	-2.1082
C	28.08447	-59.549	1.346139	H	24.80961	-60.3084	0.83119
C	26.93981	-60.3182	1.198603	O	23.43392	-57.5598	0.136635
C	25.66454	-59.6929	1.085105	O	30.0935	-60.8257	0.72867
C	25.55852	-58.3104	1.121535	O	29.55251	-53.9628	-2.09856

Optimized cartesian coordinates of S_0 for **TPA-TOS**

C	-5.66033	0.165438	0.533189	C	5.736062	0.694182	0.691786
C	-4.87857	-0.69977	1.266274	C	5.426597	-0.92879	-1.12479
C	-3.50584	-0.37453	1.541633	C	4.854529	-0.93035	-2.40365
C	-2.9535	0.791149	1.064639	C	5.409736	-1.70595	-3.41742
C	-3.77133	1.691128	0.294104	C	6.548701	-2.47435	-3.17746
C	-5.08993	1.388312	0.033534	C	7.125707	-2.46512	-1.9081
C	-5.70736	1.77671	-1.16062	C	6.567544	-1.70454	-0.88427
C	-4.98428	2.587307	-2.03584	C	6.692557	1.495935	0.056678
C	-3.61817	2.90168	-1.76539	C	7.553997	2.288536	0.810373
C	-2.9936	2.400304	-0.62397	C	7.465308	2.304458	2.201699
C	-1.52821	2.041301	-0.31945	C	6.510306	1.50996	2.835739
C	-1.59921	0.894583	0.710828	C	5.655949	0.702496	2.090509
C	-0.76096	-0.2164	0.966063	H	-5.40075	2.873266	-2.99548
C	-1.37212	-1.44231	1.429548	H	-3.04456	3.416184	-2.52848
C	-2.73534	-1.53735	1.662167	H	-0.74937	-2.32655	1.499006
C	-3.72156	-2.72032	1.600884	H	-6.30933	-3.63007	0.346059
C	-5.06663	-2.08584	1.202864	H	-7.69866	-2.08358	-0.97091
C	-6.14919	-2.56396	0.464144	H	0.967649	1.856879	1.258506
C	-6.95629	-1.66668	-0.29928	H	3.365329	1.901471	0.822788
C	-6.67111	-0.30103	-0.31343	H	3.211628	-2.21747	-0.4072
C	-6.86822	0.788994	-1.3858	H	0.816968	-2.25485	0.016125
C	0.68552	-0.20069	0.679528	H	3.979224	-0.32257	-2.59966
O	-0.55657	2.491759	-0.87798	H	4.957413	-1.69677	-4.40308
O	-3.46596	-3.89462	1.708421	H	6.982543	-3.07172	-3.97124
O	-7.67132	0.794503	-2.28585	H	8.009106	-3.0614	-1.7075
C	1.449287	0.959859	0.891473	H	7.013197	-1.70949	0.103322
C	2.812959	0.987093	0.648601	H	6.757581	1.496312	-1.02476
C	3.481662	-0.15459	0.172856	H	8.289254	2.905139	0.305021
C	2.725789	-1.32155	-0.04268	H	8.133559	2.927123	2.785563
C	1.363629	-1.33926	0.207755	H	6.437164	1.506153	3.917795
N	4.866057	-0.13336	-0.07999	H	4.92595	0.075884	2.588934

Optimized cartesian coordinates of S_1 for **TPA-TOS**

C	-5.57921	0.255054	-0.4725	C	5.777971	0.942392	-0.0797
C	-4.86005	1.424456	-0.40596	C	5.161123	-1.33913	0.566203
C	-3.49411	1.450974	-0.8531	C	4.388833	-2.43879	0.137013
C	-2.9087	0.310972	-1.35036	C	4.7538	-3.71971	0.516426
C	-3.66302	-0.90867	-1.42766	C	5.874337	-3.92575	1.324873
C	-4.96754	-0.93716	-0.99513	C	6.636532	-2.83706	1.757229
C	-5.53157	-2.07693	-0.39986	C	6.290902	-1.54926	1.383781
C	-4.73503	-3.23745	-0.37996	C	6.964041	0.592403	-0.75172
C	-3.39086	-3.20932	-0.82439	C	7.91298	1.56695	-1.01895
C	-2.80819	-2.01796	-1.29906	C	7.698581	2.887722	-0.61955
C	-1.39292	-1.48555	-1.24596	C	6.521719	3.235441	0.047354
C	-1.54287	0.025621	-1.1743	C	5.558251	2.275375	0.314088
C	-0.76235	1.044878	-0.57301	H	-5.10196	-4.13867	0.102112
C	-1.37233	2.217943	-0.06083	H	-2.77533	-4.08987	-0.66648
C	-2.76494	2.410165	-0.13411	H	-0.76016	2.912979	0.506631
C	-3.74738	3.128894	0.775507	H	-6.28262	2.775214	2.355552
C	-5.05217	2.362036	0.623325	H	-7.56811	0.690851	2.233089
C	-6.11057	2.110536	1.51435	H	1.312677	1.789716	-2.15854
C	-6.85391	0.904844	1.443575	H	3.716322	1.330008	-1.84005
C	-6.55566	-0.0753	0.48094	H	2.820908	-0.66678	1.872903
C	-6.66319	-1.59538	0.49561	H	0.423844	-0.19922	1.535365
C	0.698002	0.820036	-0.33957	H	3.531273	-2.28209	-0.50459
O	-0.35712	-2.13577	-1.13408	H	4.166761	-4.56295	0.172595
O	-3.49911	4.026334	1.566855	H	6.15019	-4.93119	1.621015
O	-7.39664	-2.27742	1.192301	H	7.492978	-2.99476	2.402422
C	1.64663	1.266353	-1.27034	H	6.858662	-0.70238	1.747822
C	2.997865	1.015467	-1.09264	H	7.112119	-0.42531	-1.09065
C	3.421369	0.291241	0.031545	H	8.816377	1.300107	-1.5552
C	2.488565	-0.13747	0.987848	H	8.444732	3.644976	-0.83085
C	1.14444	0.13483	0.799259	H	6.359175	4.258051	0.367179
N	4.796412	-0.03619	0.185528	H	4.653923	2.537324	0.848738

Optimized cartesian coordinates of T_1 for **TPA-TOS**

C	-5.62831	-0.1856	-0.53412	C	-6.64688	0.265015	0.314995
C	-4.85943	0.68107	-1.27566	C	-6.82721	-0.8028	1.391302
C	-3.48537	0.373484	-1.53003	C	0.688612	0.234452	-0.68482
C	-2.92805	-0.79609	-1.05949	O	-0.51293	-2.42229	0.942283
C	-3.7379	-1.70182	-0.2909	O	-3.45608	3.904662	-1.6887
C	-5.05509	-1.40551	-0.03296	O	-7.61358	-0.78901	2.319281
C	-5.68483	-1.7885	1.159853	C	1.42973	-0.96102	-0.81071
C	-4.94488	-2.60345	2.034127	C	2.788117	-0.99746	-0.5795
C	-3.58617	-2.90894	1.770248	C	3.472245	0.170925	-0.18528
C	-2.9427	-2.4046	0.625767	C	2.746333	1.3728	-0.04391
C	-1.50599	-2.01462	0.354297	C	1.390705	1.397234	-0.29588
C	-1.57935	-0.89523	-0.68981	N	4.850178	0.138202	0.07277
C	-0.75715	0.2496	-0.96656	C	5.703106	-0.70873	-0.68455
C	-1.35998	1.45166	-1.44395	C	5.40689	0.939246	1.105414
C	-2.73763	1.554035	-1.67655	C	4.749673	1.047748	2.341001
C	-3.71353	2.714429	-1.60736	C	5.30134	1.829984	3.346842
C	-5.04291	2.075793	-1.22534	C	6.503292	2.505839	3.135529
C	-6.13842	2.538774	-0.47812	C	7.156996	2.395212	1.907432
C	-6.93199	1.642395	0.283837	C	6.6181	1.61598	0.892913

C	6.706488	-1.44945	-0.04138	H	3.260055	2.28074	0.24373
C	7.536737	-2.27466	-0.78753	H	0.85806	2.331025	-0.17388
C	7.380684	-2.36768	-2.17116	H	3.829271	0.503714	2.510066
C	6.385592	-1.62756	-2.8101	H	4.796782	1.901852	4.302799
C	5.546804	-0.7994	-2.07642	H	6.929236	3.114754	3.923889
H	-5.36556	-2.89846	2.989584	H	8.084915	2.92751	1.735499
H	-3.01395	-3.42585	2.533165	H	7.114583	1.543778	-0.06641
H	-0.73897	2.332414	-1.55824	H	6.81264	-1.39039	1.034159
H	-6.31081	3.603967	-0.36717	H	8.300909	-2.85658	-0.28628
H	-7.68313	2.05607	0.94853	H	8.031681	-3.01324	-2.7484
H	0.917246	-1.87226	-1.08065	H	6.268603	-1.68683	-3.8855
H	3.324777	-1.93321	-0.66396	H	4.787098	-0.2087	-2.57217

5) References

S1 Nakagawa, T., Okamoto, K., Hanada, H. & Katoh, R. Probing with randomely interleaved pulse train bridges the gap between ultrafast pump-probe and nanosecond flash photolysis. *Optics Letters* **41**, 1498-1501 (2016).

S2 Reynolds, G. & Drexhage, K. New coumarin dyes with rigidized structure for flashlamp-pumped dye lasers. *Optics Communications* **13**, 222-225 (1975).

S3 Snellenburg, J. J., Laptrnok, S., Seger, R., Mullen, K. M. & van Stokkum, I. H. M. Glotaran: A Java-Based Graphical User Interface for the R Package TIMP. *Journals of Statistical Software* **49**, 1-22 (2012).

S4 Lakowicz, J. R. *Principles of fluorescence spectroscopy* (Springer, 2006).

S5 Abe, M. Diradicals. *Chemical Review* **113**, 7011-7088 (2013).

S6 Han, J., Uetake, Y., Yakiyama, Y. & Sakurai, H. Derivatization of sumanenetrione through Lewis acid-mediated Suzuki–Miyaura coupling and an unprecedented ring opening. *Chemical Communications* **59**, 4632-4635 (2023).

S7 Niwa, T., Uetake, Y., Isoda, M., Takimoto, T., Nakaoka, M., Hashizume, D., Sakurai, H., & Hosoya, T. Lewis acid-mediated Suzuki–Miyaura cross-coupling reaction. *Nature Catalysis* **4**, 1080-1088 (2021).

S8 Gaussian 16 Rev. C.01 (Wallingford, CT, 2016).

S9 Humphrey, W., Dalke, A. & Schulten, K. VMD: visual molecular dynamics. *Journal of molecular graphics* **14**, 33-38 (1996).

S10 Lu, T. & Chen, F. Multiwfn: A multifunctional wavefunction analyzer. *Journal of computational chemistry* **33**, 580-592 (2012).

S11 Samanta, P. K., Kim, D., Coropceanu, V. & Brédas, J.-L. Up-conversion intersystem crossing rates in organic emitters for thermally activated delayed fluorescence: impact of the nature of singlet vs triplet excited states. *Journal of the American Chemical Society* **139**, 4042-4051 (2017).

S12 Neese, F. Software update: The ORCA program system—Version 5.0. *WIREs Computational Molecular Science* **12**, e1606 (2022).

S13 Casanova-Paez, M. & Goerigk, L. Time-Dependent Long-Range-Corrected Double-Hybrid Density Functionals with Spin-Component nd Spin-Opposite Scaling: A Comprehensive Analysis of Singlet-Singlet and Single-Triplet Excitaion Energies *Journal of Chemical Theory and Computation* **17**, 5165-5186 (2021).

S14 Mester, D. & Kállay, M. Charge-Transfer Excitations within Density Fucntional Theory: How Accurate Are the Most Recommended Approaches? *Journal of Chemical Theory and Computation* **18**, 1646-1662 (2022).